EUROPEAN FUSION DEVELOPMENT AGREEMENT

EFDA–JET–PR(02)20

J.S. Lönnroth, V.V. Parail, G. Corrigan, D. Heading, G. Huysmans, A. Loarte,
G. Saibene, S. Sharapov and J. Spence

Integrated Predictive Modelling of the Effect of Neutral Gas Puffing in ELMy H-mode Plasmas

Integrated Predictive Modelling of the Effect of Neutral Gas Puffing in ELMy H-mode Plasmas

J.S. Lönnroth[1], V.V. Parail[2], G. Corrigan[2], D. Heading[2], G. Huysmans[3], A. Loarte[4], G. Saibene[4], S. Sharapov[2], J. Spence[2]
and contributors to the EFDA-JET workprogramme*

[1]Association EURATOM-Tekes, Helsinki University of Technology, P.O. Box 2200, 02015 HUT, Finland
[2]EURATOM/UKAEA Fusion Association, Culham Science Centre, Abingdon, Oxon OX14 3DB, UK
[3]Association EURATOM-CEA, CEA Cadarache, DRFC, Bâtiment 513, 13108 Saint-Paul-Lez-Durance, France
[4]EFDA Close Support Unit, c/o Max Planck Institut für Plasmaphysik, Boltzmannstrasse 2, 85748 Garching, Germany
** See annex of J. Pamela et al, "Overview of Recent JET Results and Future Perspectives", Fusion Energy 2000 (Proc. 18th Int. Conf. Sorrento, 2000), IAEA, Vienna (2001).*

Preprint of Paper to be submitted for publication in
Plasma Physics and Controlled Fusion

ABSTRACT.
The effect of neutral gas puffing in ELMy H-mode plasmas is studied us-ing integrated predictive transport modelling. Integrated modelling includes the plasma core, the edge transport barrier and the scrape-off layer and it is needed, because there is a strong link between these three regions. Self-consistent results are obtained by coupling the one-dimensional core transport code JETTO with the two-dimensional edge code EDGE2D. In addition, MHD stability analysis is performed on the output of the transport simulations. The results of the MHD stability analysis is used to adjust MHD stability limits in the transport modelling, so that there is a feedback loop between the transport codes and the MHD stability codes. It is shown that strong gas puffing causes a sequence of causalities involving edge density, collisionality, bootstrap current, total edge current and magnetic shear, eventually triggering a transition from second to first ideal ($n = \infty$) ballooning stability. Qualitatively, the transition from second to first ballooning stability resembles the experimentally observed transition from type I to type III ELMy H-mode with the accompanying increase in ELM frequency and deterioration of plasma confinement. Furthermore, it has been possible to reproduce the mixed type I-II ELMy H-mode, as observed in experiments.

1. INTRODUCTION

It is well-known that the edge plasma parameters influence plasma performance in many different ways. In the ELMy H-mode, which is considered a reference scenario for ITER and other burning plasma experiments, the link between edge and core is controlled by the edge transport barrier (ETB), a thin layer of improved transport characteristics. Conventionally, the plasma core, the ETB and the scrape-off layer (SOL) have been treated separately in predictive modelling with the motivation that the physics is very different in these two regions. Indeed, core transport is usually dominated by drift-type plasma tur-bulence resulting in profile stiffness, whereas anomalous transport in the ETB is reduced or even completely suppressed by strong shear in plasma rotation. The reduced transport at the edge generates a strong pressure gradient and a large edge current, both leading to periodic MHD instabilities accompanied by sharp increases of anomalous transport. These so-called edge localized modes (ELMs) are controlled by either kink / peeling or ballooning MHD instabilities [1, 2, 3, 4, 5]. Kink modes are current-driven instabilities with low toroidal mode numbers n, typically stabilized by the pressure gradient, whereas ballooning modes have higher mode numbers and are controlled by the edge pressure gradient. Finally, transport in the SOL is dominated by very fast losses along the field lines and by atomic physics processes, including interaction between the plasma and neutrals. In many studies, modelling of the plasma does not include simulation of the ETB and the SOL. Instead, the values of the relevant plasma parameters on top of the ETB are used as boundary conditions for core modelling.

However, both theory and experiments show that there is a strong link between the edge and the core, so that even a modest variation of the plasma parameters in one region can lead to a dramatic change in overall plasma performance. Profile stiffness is probably the best-known example of

such a link between core transport and edge parameters [6]. Another example of a link between the core, the ETB and the SOL is the effect of gas puffing in type I ELMy H-mode plasma [7], which will be discussed extensively in this paper. An increase in the level of neutral gas puffing, for instance, triggers a transition from type I to type III ELMs in experiments. Due to the strong link between the core, the ETB and the SOL, integrated modelling of all three regions is needed in order to obtain self-consistent results.

It should be made clear that modelling the dynamics of ELMs in the fully integrated simualations of all three plasma regions is beyond the scope of this paper. However, the dynamics of ELMs are modelled in stand-alone core simulations closely linked to the fully integrated runs. In an ELMy H-mode plasma, the pressure gradient and the associated bootstrap current slowly build up until one of these two parameters reaches a critical level, whereby an ELM disruption occurs. Each ELM temporarily increases all transport coefficients in the pedestal region causing the pressure gradient and bootstrap current to drop back to a low level. The ELM cycle is repeated periodically, as illustrated in Fig.1. The figure shows a possible scenario of ELMs triggered by a critical pressure gradient. In the fully integrated modelling presented in this paper, the plasma is allowed to evolve toward an ELM, but the analysis is carried out before the conditions for an ELM disruption are reached.

The integrated predictive transport modelling of ELMy H-mode JET plasmas presented in this paper has been performed using a suite of JET transport codes. Core modelling has been done with the 1.5D transport code JETTO [8], whose output is linked to a suite of MHD stability codes. Since core modelling alone is not sufficient, the edge transport code EDGE2D/NIMBUS [9] has been used for 2D modelling of the SOL. Finally, both core and edge have been modelled self-consistently using COCONUT, a coupling of EDGE2D and JETTO.

The MHD stability analysis has been performed using the codes IDBALL, HELENA and MISHKA [10]. IDBALL and HELENA have been used for $n = \infty$ ballooning stability analysis. HELENA, which is an MHD equilibrium solver, also acts as a link between JETTO and MISHKA. Finally, MISHKA is used for kink / peeling and finite n ballooning stability analysis. To be specific, a version of MISHKA called MISHKA-1 is used in this study. This version is based on ideal MHD and does not take into account the ω^* effect.

The inclusion of drift effects [11] in the analysis will be discussed elsewhere.

The plan for this paper is as follows: The simulation model is described in Sec. 2. In Sec. 3, some experimental observations of relevance to this study are discussed. Section 4 is devoted to integrated predictive transport modelling. First, it is explained how integrated predictive modelling unravels a sequence of causalities which shows how strong gas fuelling can affect MHD stability. Some explanations for the experimental obser-vations are proposed. Finally, integrated predictive transport modelling of a gas puffing scan is discussed in detail. Section 5 is devoted to MHD stability analysis of some of the scenarios from the gas puffing scan. The experimental observations outlined in Sec. 3 are given explanations based on the modelling and MHD stability analysis. The paper is concluded with a short summary and discussion.

2. SIMULATION MODEL

2.1 JETTO

In this work, the empirical JET transport model, a so-called mixed Bohm / gyro-Bohm model [12], has been used in simulations with JETTO, including integrated simulations with JETTO being part of the COCONUT code. The Bohm and the gyro-Bohm scalings in the JET model are given by the following contributions to the diffusivity:

$$\chi^{\text{Bohm}} = \rho_s c_s q^2 \, a \left| \frac{\partial (n_e T_e)/\partial r}{n_e T_e} \right| \Delta_{Te}\,(0.8a) \tag{1}$$

$$\chi^{\text{gyro-Bohm}} = \rho_s c_s^2 \left| \frac{\partial T_e/\partial r}{T_e} \right|. \tag{2}$$

Here,ρ_s is the gyro radius, c_s is the sound speed, q is the safety factor, a is the plasma minor radius, n_e is the electron density, T_e is the electron temperature and the dimension less quantity Δ_{Te} (0.8a) = (T_e(0.8a) – T_e(a)) / T_e(a) is the relative temperature difference with respect to the plasma edge. The ion and electron thermal diffusivities are given by

$$\chi_i^{\text{JET}} = 1.6 \times 10^{-4}\, \chi^{\text{Bohm}} + 1.75 \times 10^{-2}\, \chi^{\text{gyro-Bohm}} + \chi_i^{\text{neo}} \tag{3}$$

$$\chi_e^{\text{JET}} = 8 \times 10^{-5}\, \chi^{\text{Bohm}} + 3.5 \times 10^{-2}\, \chi^{\text{gyro-Bohm}}, \tag{4}$$

where χ_i^{neo} is the neo-classical ion thermal diffusivity [13], and the charged particle diffusivity by

$$D_i^{\text{JET}} \sim \frac{\chi_i \chi_e}{\chi_i + \chi_e} \tag{5}$$

The Bohm term in the model includes both electron and ion transport as well as a non-local factor accounting for the instantaneous effect of perturbations starting at the plasma edge, such as ELMs. The gyro-Bohm term makes its largest contribution in the deep core.

JETTO explicitly takes the region with the ETB into account. It is assumed that anoma-lous transport is completely suppressed within the ETB, so that the only remaining transport is neo-classical. The transport coefficients are thus suddenly reduced to the neo-classical level at the top of the ETB. This is illustrated in Fig.2, which shows how the transport coefficients vary in the radial direction in a typical simulation. The width of the ETB is considered an external fixed parameter, which is calculated using recently developed theory-based models [14]. JETTO has a fixed boundary solver of the Grad-Schafranov equation, which generates equilibria consistent with the predicted temperature and pressure profiles in the core. JETTO includes an implementation for dynamic modelling of ELMs [15]. Although the MHD stability code MISHKA can perform stability analysis against both kink and ballooning modes, ballooning stability is used as a trigger for ELMs in this paper. An ELM is triggered when the critical pressure gradient defined by an MHD stability limit is reached. In JETTO, one can specify a value for the normalized critical pressure gradient c.

In this work, the following normalization is used:

$$\alpha = - \frac{2\mu_0 q^2}{B_0^2 \epsilon} \frac{dp}{d\rho} \tag{6}$$

Here, μ_0 is permeability of vacuum, q is the safety factor, B_0 is the magnetic field on the magnetic axis, ε is the inverse aspect ratio, p is the pressure and ρ is the toroidal flux co-ordinate. During ELMs, all transport coefficients within the ETB are multiplied by given multiplication factors, typically between 100 and 1000, during a given length of time, typically between 10^{-4}s and 10^{-3}s. As discussed earlier, ELMs can also be triggered by current-driven kink modes. JETTO includes an implementation for current-triggered ELMs as well, but in this work it is assumed that the ELMs are controlled by the pressure gradient.

2.2 EDGE2D

The edge transport code EDGE2D works on a two-dimensional computational grid for the SOL. The grid covers the whole poloidal angle around the vacuum vessel as well as the target and private regions next to the divertor and the X-point. In stand-alone simulations with EDGE2D, the two-dimensional grid can be extended beyond the SOL to include the whole ETB. A typical boundary condition in a stand-alone simulation is that the charged particle fluxes from the core into the simulation region equals the neutral particle fluxes from the simulation region into the core plus any assumed particle sources in the core. In addition, the heat fluxes at the boundary toward the core are given as boundary conditions. In stand-alone edge modelling with EDGE2 as well as in integrated modelling with COCONUT, perpendicular transport in the SOL is kept at the low neo-classical level, as shown in Fig. 2. Longitudinal transport is assumed to be classical.

2.3 COCONUT

In a coupled COCONUT run, the two-dimensional EDGE2D grid extends radially out-ward from the separatrix, whereas JETTO simulates the entire core region up to the separatrix in one dimension. Here, the width of the EDGE2D simulation region is typically about 1.5 cm at the mid-plane. The fact that the SOL is so narrow in the simulations does not affect the results significantly. In a COCONUT run, JETTO calculates the heat fluxes and transport coefficients in the core and passes their values at the separatrix as boundary conditions for EDGE2D, whereas EDGE2D calculates the corresponding quantities in the SOL and passes their separatrix values as boundary conditions for JETTO. Both codes are called at each time step. Since the core is modelled in one dimension and the edge in two dimensions, the boundary conditions have to be treated as averages. In a COCONUT run, the two-dimensional grid for EDGE2D extends a short distance inside the separatrix, so that there is a small overlap with the simulation region of JETTO. This makes it straighforward to distribute the one-dimensional heat fluxes and transport coefficients from JETTO over the whole poloidal angle for EDGE2D and to average the corresponding two-dimensional quantities from EDGE2D over the poloidal angle for JETTO.

2.4 MHD STABILITY CODES

The MHD stability codes MISHKA and IDBALL are run using the output of stand-alone JETTO simulations. However, in order to keep the analysis self-consistent the separatrix values of e.g. density and temperature from integrated self-consistent COCONUT runs are used as boundary conditions for the JETTO runs on which the MHD stability analysis is performed. The results of the MHD stability analysis, on the other hand, are used to set stability limits, e.g. an appropriate value for the critical pressure gradient, in modelling with JETTO and COCONUT. In this way, there is a feedback loop between the trans-port codes and the MHD stability codes and the modelling can be considered integrated modelling of both transport and MHD stability.

3. EXPERIMENTAL BACKGROUND

The sensitive dependence of plasma performance on the edge parameters is very well demonstrated in experiments with external gas fuelling in type I ELMy H-mode plasma [7]. From experiments, it is known that plasma easily accommodates modest gas puffing, e.g. a neutral influx of $\Gamma = 3\times10^{22}\,s^{-1}$ in the case of JET. Higher levels of gas puffing can trigger a transition from type I to type III ELMs with a dramatic increase in the ELM frequency followed by a deterioration of plasma confinement.

A comparison between JET Pulse No's: 53298 and 52739 can serve as an illustrative example. Both discharges are high-triangularity (δ = 0.5) shots with very similar magnetic configurations. Figure 3 shows some characteristic time traces of the discharges. As shown in frame (a) the heating power is essentially the same in both shots, P_{tot} = 16MW. Moreover, the magnetic field shown in frame (b) and the plasma current shown in frame (c) are also essentially the same in both discharges, B_0 = 2.7T and I = 2.5MA, respectively. Hence, the major differences between the two shots are due to the different levels of external neutral gas fuelling shown in frame (d), $\Gamma = 0$ and $\Gamma = 6\times10^{22}\,s^{-1}$ for Pulse No's: 53298 and 52739, respectively. The different characteristics of the two discharges are perhaps best illustrated by comparing frames (e) and (f), which are time traces of D-alpha emission for shots 53298 and 52739, respectively. Shot 53298 with zero gas fuelling is characterized by low-frequency type I ELMs, whereas shot 52739 with strong gas fuelling features more frequent type III ELMs. The difference in ELM frequency is significant. The increased ELM frequency in Pulse No: 52739 is accompanied by a deterioration of plasma confinement, as illustrated in frame (g) showing the confinement enhancement factor H98Y. As will be shown, these experimental observations can be explained by in-tegrated predictive modelling.

4. RESULTS OF INTEGRATED PREDICTIVE TRANSPORT MODELLING

4.1 SEQUENCE OF CAUSALITIES UNRAVELLED BY INTEGRATED PREDICTIVE TRANSPORT MODELLING

Integrated predictive transport modelling unravels a chain of causalities which can explain the experimentally observed transition from type I to type III ELMs and the subsequent increase in ELM frequency. An increase in neutral gas puffing influences the SOL in the first place. To begin with, it

should be understood that only a minor fraction of the total gas puff actually penetrates the separatrix. The high-triangularity ELMy H-mode JET Pulse No's: 53298, 53299 and 52739 have been used as templates for a gas puff scan with the integrated code COCONUT. Pulse No: 53299 differs from Pulse No's: 53298 and 52739 only with respect to the level of gas puffing: $\Gamma = 4.5 \times 10^{22}\,s^{-1}$ for Pulse No: 53299. For each level of neutral gas puffing, the total influx of neutral particles from the SOL through the separatrix into the core has been computed. The results of this study are shown in Fig.4, which shows the total influx of neutrals through the separatrix as a function of the total puff rate. The figure reveals that as most of the neutrals are ionized in the SOL, only a small fraction of the total gas puff actually penetrates all the way through the separatrix. In fact, the neutral influx through the separatrix is between one and two orders of magnitude smaller than the total rate of gas fuelling and seems to decrease with increasing puff rate. [16]

The fact that only a small fraction of the total neutral gas puff actually penetrates the separatrix means that an excess of particles is accumulated in the SOL before a balance is reached. Hence, the density in the vicinity of the separatrix increases sharply for increased gas puffing. Deeper in the core, the density increases much more slowly. The increase in density shown in frame (a) in Fig.5. Figure 5, which illustrates a sequence of causalities revealed by integrated predictive modelling, contains the profiles of a number of relevant plasma parameters in three COCONUT runs with different levels of gas puffing:$\Gamma = 0$, $\Gamma = 4 \times 10^{22}\,s^{-1}$ and $\Gamma = 1 \times 10^{23}\,s^{-1}$. Frame (b) in Fig. 5 shows that both the ion and electron temperatures at the separatrix decrease for increasing gas puffing in order to keep the pressure and pressure gradient constant. Collisionality at the edge, on the other hand, increases with the edge density. To a first approximation, the bootstrap current I_{bs} scales as $I_{bs} \sim 1/(1+\nu^*)$, where ν^* is the collisionality. As a result of the increased collisionality at the edge, there is a significant decrease of the bootstrap current with increasing gas puffing, as shown in frame (c) in Fig. 5. Hence, the edge current, which comprises of both bootstrap and Ohmic current, decreases significantly, as illustrated in frame (d) in Fig. 5. Magnetic shear, plotted in frame (e) in Fig. 5, increases with decreasing edge current. It is known that magnetic shear controls MHD stability in general and ideal ($n = \infty$) ballooning stability in particular. In this way, external gas fuelling can play a significant role in controlling ballooning stability.

This effect on ballooning stability is illustrated in Fig. 6, which shows a typical $n = \infty$ ballooning stability diagram with the normalized pressure gradient on the horizontal axis and magnetic shear on the vertical one. The figure shows how predictive modelling can explain the experimentally observed transition from type I to type III ELMs and increase in ELM frequency: Increasing magnetic shear without changing the normalized pressure gradient causes the operational point to be pushed from the second ballooning stability region into the ideal ballooning unstable region. However, a real physical system cannot remain in a state with a combination of the pressure gradient and magnetic shear resulting in an instability. Hence, the pressure gradient drops until the system becomes stable, i.e. until the operational point reaches the first stability region. In this way, strong gas puffing can trigger a transition from second to first n = 1 ballooning stability with a subsequent reduction in the critical level of the pressure gradient. This topic will be discussed in more detail later in this paper.

4.2 GAS PUFF SCAN

In this section, the results of integrated transport modelling of a gas puff scan involving six different levels of neutral gas puffing are presented. The simulations have been performed using the coupled code COCONUT on a computational grid generated for JET Pulse No: 53298. Some results of the gas puff scan are presented in Table 1. Figure 7 shows the ion density profiles in a region covering the SOL, the ETB and part of the core for all six simulations in the scan. The separatrix is located at R = 3:90 m, where the density gradient changes. The other change in the density gradient visible in some of the profiles corresponds to the top of the ETB at R = 3:855 m. As explained earlier, the edge density increases with increasing gas puffing, whereas the edge temperature and the neutral influx through the separatrix decrease. The corresponding ion temperature profiles are shown in Fig. 8. Attention should be paid to the fact that the separatrix density reaches very high values for strong levels of gas puffing, e.g. n_i (ρ = 1) = $8.4 \times 10^{19}\,m^{-3}$ for a puff rate of $\Gamma = 1 \times 10^{23}\,s^{-1}$. Reliable experimental data on the density, however, is scarce. At JET, there are basically two types of diagnostic data available for the density: Edge Lidar (Thomson scattering) data and target probe data, but methods have a number of known problems. With edge Lidar, the position of the separatrix with respect to the data is not measured but reconstructed using the magnetic equilibrium code EFIT and the density gradient in the vicinity of the separatrix is large. Hence, the uncertainty of the measurements in the vicinity of the separatrix becomes large. The target probe data, on the other hand, exists only for the target regions. In order to obtain data for the outer mid-plane region, some kind of mapping technique has to be used.

The difficulty of comparing the predictive transport simulations with experimental data is evident in Fig. 9, which shows Edge Lidar data for the electron density and electron temperature for JET Pulse No: 53299 with a gas puffing rate of $\Gamma = 5 \times 10^{22}\,s^{-1}$. It should be emphasized that the true location of the separatrix does not necessarily coincide with zero on the horizontal scale. In fact, the location of the separatrix with respect to the data in the plots is unknown by a few centimetres. This is the level of uncertainty in the magnetic equilibrium code EFIT used to reconstruct the flux surfaces. Since the density increases from 0 to $8 \times 10^{19}\,m^{-3}$ in just 4 cm, the uncertainty in the separatrix density is huge. The separatrix densities n_i (ρ = 1) = $4.40 \times 10^{19}\,m^{-3}$ and n_i (ρ = 1) = $6.65 \times 10^{19}\,m^{-3}$ obtained in the simulations with $\Gamma = 4 \times 10^{22}\,s^{-1}$ and $\Gamma = 6 \times 10^{22}\,s^{-1}$ respectively, easily fit into the range of uncertainty obtained from the data. A comparison of target probe data with target data from COCONUT does not succeed much better, because the uncertainty in the target probe data is large as well.

In order to investigate the possibility that the results of the integrated modelling would have been adversely affected by some inappropriately chosen simulation parameter, a sensitivity study with respect to a number of simulation parameters was carried out. To begin with, one of the COCONUT runs with modest gas puffing ($\Gamma = 4 \times 10^{22}\,s^{-1}$) was matched by a stand-alone EDGE2D run using the heat fluxes from the COCONUT run as boundary conditions. Then, the following "perturbations" were separately imposed on the starting scenario: The heat fluxes specified as boundary conditions were increased by up to three times, the transport coefficients given by

COCONUT were also increased by up to three times, radiation from the SOL was increased by up to two times and recycling was reduced by up to 2.5%. In each of the extreme cases, the effect on the density in the SOL was still modest. The largest reduction in the separatrix density resulted from increasing the transport coefficients three times and from reducing recycling by 2.5%, whereby the density dropped by 20%. The change in heat fluxes and radiation caused the density to drop by less than 15%. These results show that the density obtained in the predictive transport simulations is not very sensitive to any other input parameter than the rate of gas puffing. It was also studied how the location and width of the region with gas puffing affects the density in the SOL. Since the particles are relatively free to move along the field lines, the local density remains relatively insensitive to the poloidal location of the puffing region.

5. MHD STABILITY ANALYSIS

Using MHD stability codes MISHKA and HELENA, MHD stability analysis was performed for some of the scenarios discussed in the preceding section. Three different levels of gas puffing were included in the MHD stability analysis: $\Gamma = 0$, $\Gamma = 4 \times 10^{22}\,s^{-1}$and $\Gamma = 1 \times 10^{23}\,s^{-1}$. In order to maintain self-consistency, the analysis was based on the self- consistent COCONUT runs. To begin with, JETTO was run with the relevant separatrix values for the density and temperature given in Table 1 as boundary conditions. In this way, the MHD stability analysis was done on fully self consistent JETTO simulations. The dynamics of ELMs were not included in the analysis. The results of the MHD stability analysis are illustrated in Figs. 10, 11 and 12 corre-sponding to gas puffing rates $\Gamma = 0$, $\Gamma = 4 \times 10^{22}\,s^{-1}$and $\Gamma = 1 \times 10^{23}\,s^{-1}$, respectively. The plots have been obtained by running HELENA and MISHKA on a set of equilibria obtained by repeatedly changing the edge pressure gradient and edge current within the ETB. Each combination of edge pressure gradient and edge current translates into a given level of magnetic shear. For each combination, the mode number of the most unstable peeling or finite n ballooning mode as calculated by MISHKA has been printed onto the plots in a co-ordinate system with the normalized pressure gradient α on the horizontal axis and magnetic shear s on the vertical one. Whenever no instabilities have been found, the relevant location on the plot has been left blank. In addition, the $n = \infty$ ballooning instabilities as calculated by HELENA have been marked with crosses on the plots. One can easily make out four distinct regions on the plots, each of which has been marked with a different shade of grey: a region with no instabilities, a region in which the low n kink instability is dominant, a region in which the medium n ballooning / peeling insta-bility dominates and the $n = \infty$ ballooning unstable region. In most cases, the latter two regions partially overlap each other. Finally, the plots show the location of the operational point, i.e. the point with unperturbed edge current and edge density, for a few different magnetic surfaces.

A few things should be noted. Firstly, the MHD stability analysis done with MISHKA has been limited to toroidal mode numbers n smaller than or equal to 14 due the limitations of modern computers. The computing time and memory requirements namely increase with the square of n, so that it quickly becomes more and more demanding to do the analysis for higher and higher mode

numbers. Because of the limited range of the analysis, it is quite probable that n = 14is not actually the most unstable mode in all the cases indicated on the plots. It can be expected that some mode with higher mode number is actually more unstable at many of the locations marked with an n = 14instability. Secondly, it should be noted that the stability diagram varies slightly as a function of the magnetic surface, so that the stability boundaries look slightly different for each magnetic surface. Shown is the stability diagram for $\rho = 0{:}95$, which corresponds to the top of the ETB.

When comparing Figs. 10, 11 and 12, one should keep in mind the conclusions of Sec. 4.1, such as the fact that increasing gas puffing leads to decreasing bootstrap current and total edge current and increasing magnetic shear. Indeed, the case with zero gas puffing illustrated by Fig. 10 is very kink unstable, because the edge current is high due to the low edge density. However, despite the strong kink instability there is still a gap with access to second $n = \infty$ ballooning stability, but it closes for $s < 2$. For increasing ρ, the operational point moves from the first ballooning stability region into the second ballooning stability region without touching the $n = \infty$ ballooning stability limit. The system remains in the second stability region for all magnetic surfaces within the ETB. The maximum operational α obtained in this scenario is limited by a region of finite n ballooning / peeling instability.

In Fig. 11 corresponding to the scenario with the intermediate level of gas puffing, the system is more kink stable, because the edge current is significantly smaller than in the case with zero gas fuelling. Access to second stability opens readily, since the kink instability is suppressed. Again, the maximum operational α, in this case $\alpha \approx 6$ plasma is deined by a region of n = 14 ballooning instability. The radial localization of these modes is approximately equal to the width of the ETB. For the magnetic surface corresponding to the top of the ETB, the system is in the second stability region. However, because the edge current is small, magnetic shear increases dramatically at the edge. Therefore, the plasma is $n = \infty$ ballooning unstable at the very edge. Indeed, it seems to be a ubiquitous feature that the edge ($\hat{} > 0{:}97$) is always unstable for an intermediate or strong level of gas puffing. This causes ELM activity resembling the experimentally observed mixed type I-II ELMy H-mode in JET [17], as will be discussed later.

In the case with the strongest gas fuelling illustrated by Fig. 12, the edge current is vanishingly small everywhere within the ETB, whereby magnetic shear is strong. Therefore, access to second stability is closed. Instead, the operational point is pushed directly from the first stability region into the ideal ballooning unstable region. The whole ETB is unstable. It should also be noted that the kink instability is very much suppressed because of the small edge current.

5.1 TRANSITION FROM SECOND TO FIRST BALLOONING STABILITY

As discussed earlier, the plasma cannot remain in a state with a combination of pressure gradient and magnetic shear that results in an MHD instability. For the case with the strongest gas fuelling illustrated by Fig.12, this would mean that the pressure gradient would actually never exceed the first stability limit at $\alpha \approx 3.5$ due to the triggering of ELMs. Thus, the operational point would always be in the first ballooning stability region. Similarly, the operational point would remain in

the second ballooning stability region for magnetic surfaces within the ETB in the scenarios with lower levels of gas fuelling illustrated by Figs. 10 and 11. As magnetic shear is lower in these cases, the pressure gradient can take values up to $\alpha \approx 6$ defined by the finite n ballooning stability limit. From the discussion here, it is clear that an increase from low to high levels of neutral gas puffing at some point causes the operational point to move from the second to the first ballooning stability region, whichever part of the ETB is considered. Qualitatively, this means that a sufficiently strong increase in neutral gas puffing can trigger a transition from second to first ballooning stability.

The dynamics of the transition from second to first ballooning stability has been investigated with JETTO by varying the level of gas puffing and using a critical pressure gradient corresponding to the relevant stability limit. A run with modest gas puffing $\Gamma = 2 \times 10^{22}\,s^{-1}$ and critical pressure gradient $\alpha_c = 6$ corresponding to the finite n ballooning stability limit has been compared with a run with strong gas puffing $\Gamma = 1 \times 10^{23}\,s^{-1}$ and critical pressure gradient $\alpha_c = 3.5$ corresponding to the first stability limit. The ELM frequency in the latter case is about an order of magnitude larger than in the former case. This is illustrated in Fig. 13, which shows the ion thermal conductivity χ_i as a function of time in both cases. It is easy to understand why the ELMs necessarily become more frequent for a smaller value of the critical pressure gradient: The smaller the critical pressure gradient is, the less time it takes for the pressure gradient to build up to the critical value.

The increase in ELM frequency is very similar to what has been observed in experiments with strong gas puffing. Hence, it can be concluded that it might be qualitatively possible to explain the experimentally observed transition from type I to type III ELMy H-mode triggered by strong gas puffing as a transition from second to first ballooning stability. The experimentally observed increase in ELM frequency seems to be due to the fact that the inherent critical pressure gradient of the system decreases in the transition from second to first ballooning stability. Finally, the deterioration in plasma confinement associated with the transition from type I to type III ELMs might also be explained by the decrease in the critical pressure gradient, which leads to more frequent MHD instabilities and thus ELMs. It is worth noting that the first ballooning stability boundary can be controlled by resistive rather than ideal ballooning modes in highly collisional plasma [18]. This can further reduce the achievable level of critical pressure gradient below $\alpha \approx 3.5$. Other effects such as differential plasma rotation or diagmagnetic effects mat affect the stability boundaries as well.

5.2 MIXED TYPE I-II ELMY H-MODE

As mentioned before, the result illustrated in Fig. 11 implies an explanation for experimentally observed mixed type I-II ELMy H-mode activity. In order to simulate plasmas with mixed type I-II ELMy H-mode, a slight modification was made to the ELM model in JETTO. The ETB was divided into two regions, an inner region corresponding to the part of the ETB in the second stability region in Fig. 11 and an outer region corresponding to the unstable edge. In accordance with the previous discussion on the behaviour of the critical pressure gradient, $\alpha \approx 6.0$ was used in the inner region and in the $\alpha \approx 3.5$ outer region. The enhancement of transport due to ELMs originating in the inner region was applied over the whole ETB, whereas the ELMs in the outer region were

confined to the outer region itself only. This is consistent with the understanding that the $n = \infty$ ballooning limiting stability near the very edge are now more localized than the finite n ballooning modes determining stability closer to the top of the ETB.

Using the ELM model described here, it was possible to qualitatively reproduce the experimentally observed mixed type I-II ELMy H-mode in stand-alone JETTO simulations. The result is shown in Fig.14, which is derived from a simulation with the intermediate level of gas puffing $\Gamma = 4 \times 10^{22}\,s^{-1}$. Frame (a) shows frequent "small" type II ELMs occurring in the edge region of the ETB with α_c = 3.5, whereas frame (b) illustrates less frequent "large" type I ELMs originating in the inner region of the ETB with α_c = 6.0. In frame (c), both these plots of the ion thermal conductivity as a function of time have been included in the same composite plot. Since the large type I ELMs extend over the whole pedestal, this is what χ_i actually looks like as a function of time in the outer region of the ETB.

Frame (d) in Fig. 14 shows the energy content of the plasma as a function of time. It demonstrates that the energy content is essentially controlled by the "large" type I ELMs, which remove about 8% of the plasma energy per ELM. The energy loss during the "small" type II ELMs is negligible compared to this. Such behaviour is characteristic for a model in which the "large" type I ELMs extend over the whole ETB. The plasma energy content in the simulation with mixed type I-II ELMy H-mode has been compared to that in simulations corresponding to pure type I ELMy H-mode (α_c = 6.0) and pure type III ELMy H-mode (α_c =3.5), as illustrated in frame (d) in Fig. 14. The comparison demonstrates that the energy content in the case with mixed type I-II ELMs is significantly higher than in the case with type III ELMs and nearly as high as in the case with type I ELMs. Frame (e) shows the confinement factor H89 as a function of time and a similar comparison as in frame (d) for the three different types of ELMy H-mode plasma. Again, the same trend is evident. Plasma confinement in the case with mixed type I-II ELMy H-mode is nearly as high as in the case with type I ELMy H-mode and significantly higher than in the case with type III ELMy H-mode.

6. SUMMARY AND DISCUSSION

In this work, integrated predictive modelling of ELMy H-mode JET plasmas has been per-formed using the integrated transport code COCONUT, which is a coupling of the JET transport codes EDGE2D and JETTO for edge (SOL) and core modelling, respectively. Integrated modelling is needed, because separate stand-alone core and edge modelling does not yield self-consistent results. It has been shown through integrated predictive modelling that external gas fuelling can very sensitively affect ballooning and peeling/kink stability via its influence on edge density, collisionality, bootstrap current, total edge current and magnetic shear. Modelling with COCONUT also shows that very high edge densities can be reached with strong external gas fuelling. Moreover, the modelling also reveals that only a minor fraction of the total neutral gas puff injected at the edge actually penetrates all the way through the separatrix. The simulation results are consistent with the experimental data that is avaiable for scenarios resembling those simulated here. However, the accuracy of the edge data for JET is poor, largely due to the uncertainty in the position of the separatrix. MHD stability analysis has been performed on JETTO runs using boundary conditions calculated self-consistently by

COCONUT. For low levels of gas puffing, the plasma is very kink unstable. It has been shown that the plasma can gain access to second n = ∞ ballooning stability in many cases, such as with modest gas puffing. The transition to second stability can be controlled either by the peeling and the finite n ballooning modes or by infinite n ballooning stability. It has also been demonstrated that strong gas puffing can trigger a transition from second to first ballooning stability, which causes a dramatic decrease in the inherent critical pressure gradient of the system. As a result of this, the ELM frequency increases dramatically. The result implies that it might be possible to explain the experimentally observed transition from type I to type III ELMy H-mode triggered by strong gas puffing as well as the subsequent increase in ELM frequency and deterioration of plasma confinement as a transition from second to first stability. Furthermore, it has been possible to qualitatively reproduce the experimentally observed mixed type I-II ELMy H-mode in transport simulations.

REFERENCES

[1]. G.T.A. Huysmans, T. Hender, B. Alper, Nucl. Fusion **38** 179 (1998).

[2]. J.W. Connor, R.J. Hastie, H.R. Wilson, R.L. Miller, Phys. Plasmas **5** 2687 (1998).

[3]. B.N. Rogers, J.F. Drake, Phys. Plasmas **6** 2797 (1999).

[4]. R.J. Hastie, P.J. Catto, J.J. Ramos, Phys. Plasmas **7** 4561 (2000).

[5]. P.B. Snyder, H.R. Wilson et al., Phys. Plasmas **9** 2037 (2002).

[6]. A.M. Dimits, G. Bateman, A.A. Beer et al., Phys. Plasmas **7** 969 (2000).

[7]. G. Saibene et al., Proc. 28th EPS Conference on Plasma Physics and Controlled Fusion, Madeira, Portugal, 18-22 June 2001.

[8]. G. Cennachi, A. Taroni, JET-IR(88)03 (1988).

[9]. R. Simonini et al., Contrib. Plasma Phys. **34** 368 (1994).

[10]. A.B. Mikhailovskii et al., Plasma Phys. Rep. **23** 844 (1997).

[11]. G.T.A. Huysmans, S.E. Sharapov, A.B. Mikhailovskii, W. Kerner, Phys. Plasmas, **10** 4292 (2001).

[12]. M. Erba et al., Plasma Phys. Controlled Fusion **39** 261 (1997).

[13]. W.A. Houlberg, K.C. Shaing, S.P. Hirshman, M.C. Zarnstorff, Phys. Plasmas **4** 3231 (1997).

[14]. T. Onjunet al. submitted to Phys. Plasmas (2002).

[15]. V.V. Parail et al., Proc. 27th EPS Conference on Plasma Physics and Controlled Fusion, Budapest, Hungary, 19-23 June, 2000.

[16]. JET Team (presented by A. Taroni), Proc. 16th IAEA International Conference on Fusion Energy, Montreal, Canada 7-11 October 1996.

[17]. G. Saibene, R. Sartori, A. Loarte et al. submitted to Plasma Phys. Control. Fusion (2002).

[18]. A.H. Glasser, J.M. Greene, J.L. Johnson, Phys. Fluids **18** 875 (1975).

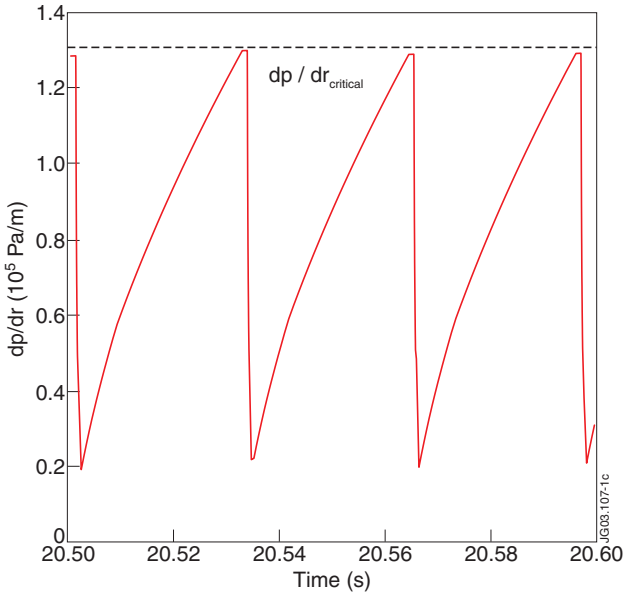

Figure 1: The pressure gradient as a function of time in two predictive simulations with different levels of gas puffing, $\Gamma = 0$ (full line) and $\Gamma = 4 \times 10^{22}\ s^{-1}$ (dashed line). For each case the critical pressure gradient is different. The analysis is carried out for the same level of the pressure gradient for each scenario, as indicated.

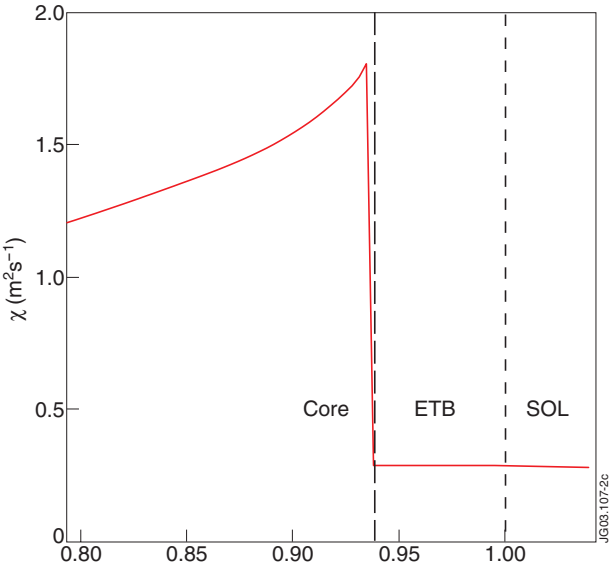

Figure 2: The ion transport coefficient χ_i as a function of the toroidal flux co-ordinate ρ in a typical COCONUT simulation with strong gas puffing ($\Gamma = 1 \times 10^{23}\ s^{-1}$). In the core, a Bohm / gyro-Bohm model is used. Transport within the ETB is reduced to a neo-classical level. In integrated modelling with COCONUT and stand-alone edge modelling with EDGE2D, transport in the SOL is kept at a low neo-classical level as well.

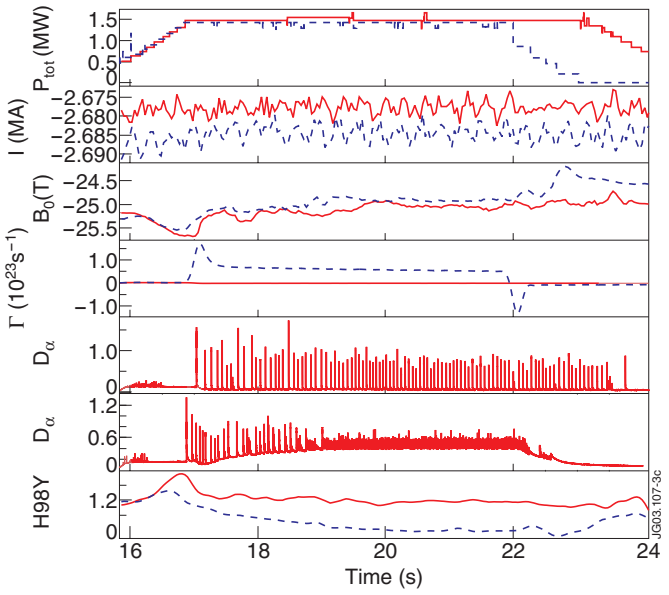

Figure 3: A comparison between JET Pulse No's: 53298 and 52739. The figure contains the following time traces: (a) Neutral beam heating power. (b) Magnetic field. (c) Plasma current. (d) Neutral gas fuelling. (e) D-alpha emission in shot 53298. (f) D-alpha emis-sion in Pulse No: 52739. (g) Confinement enhancement factor. In frames (a), (b), (c), (d) and (g) the full line corresponds to Pulse No: 53298 and the dashed one to Pulse No: 52739.

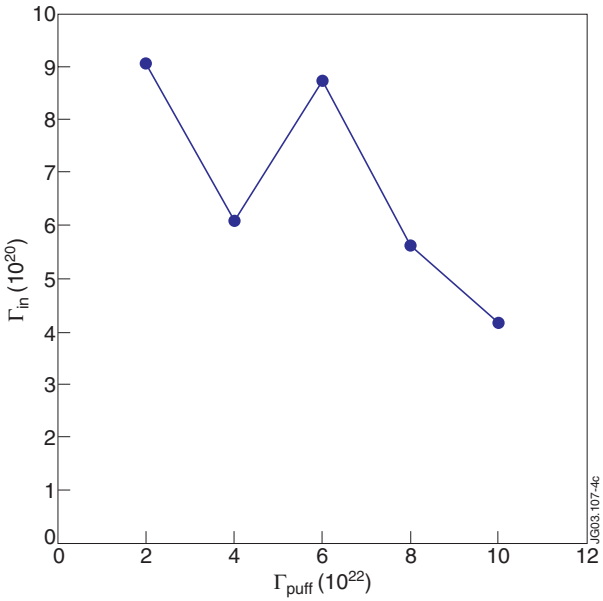

Figure 4: The total influx of neutrals through the separatrix as a function of the total rate of neutral gas puffing in integrated predictive simulations using the geometry of JET Pulse No's:53298, 53299 and 52739.

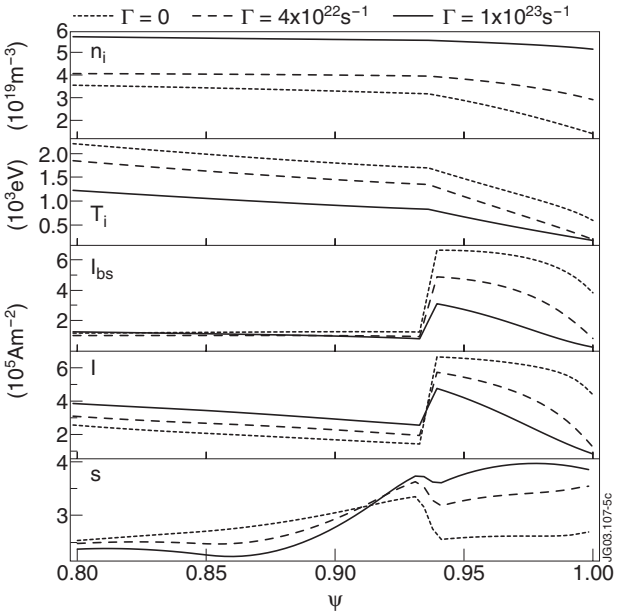

Figure 5: (a) Ion density, (b) ion temperature, (c) bootstrap current, (d) total plasma current and (e) magnetic shear in three integrated predictive transport simulations with different levels of gas fuelling $\Gamma = 0$ (dotted line), $\Gamma = 4 \times 10^{22}$ s^{-1}(dashed line) and $\Gamma = 1 \times 10^{23}$ s^{-1} (full line).

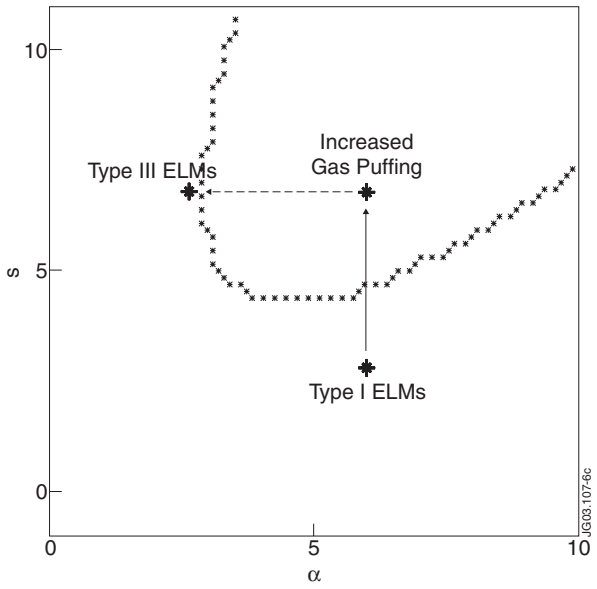

Figure 6: A typical ideal (n = ∞) ballooning stability diagram with the normalized pressure gradient on the horizontal axis and magnetic shear on the vertical one. The curve in the figure specifies the ballooning stability limit. Predictive modelling shows that strong gas puffing can trigger a transition from second to first n = ∞ ballooning stability. Increasing shear pushes the operational point into the unstable region. However, a physical system cannot remain in an unstable state. Hence, the pressure gradient decreases until the operational point reaches the first stability region.

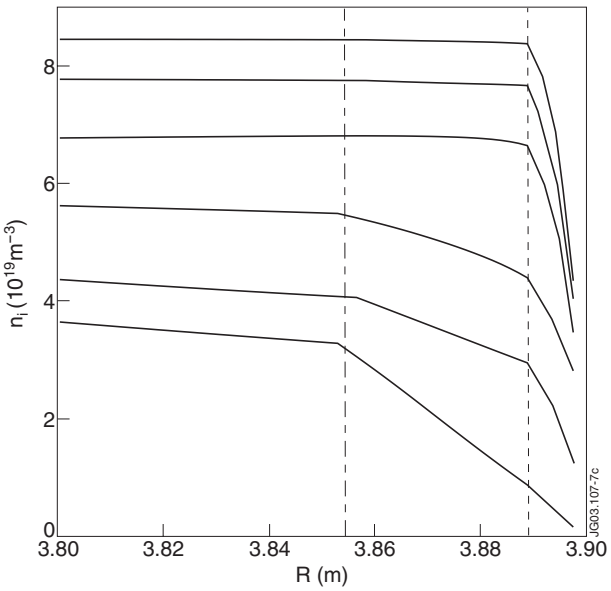

Figure 7: Ion density as a function of the major radius in integrated predictive simulations with different levels of external neutral gas puffing. Counting from top to bottom in the figure, the ion density profiles correspond are from simulations with the following levels of gas puffing: $\Gamma = 1 \times 10^{23}$ s^{-1}, $\Gamma = 8 \times 10^{22}$ s^{-1}, $\Gamma = 6 \times 10^{22}$ s^{-1}, $\Gamma = 4 \times 10^{22}$ s^{-1}, $\Gamma = 2 \times 10^{22}$ s^{-1} and $\Gamma = 0$. The position of the top of the ETB has been indicated with a chain line and the separatrix with a dashed line.

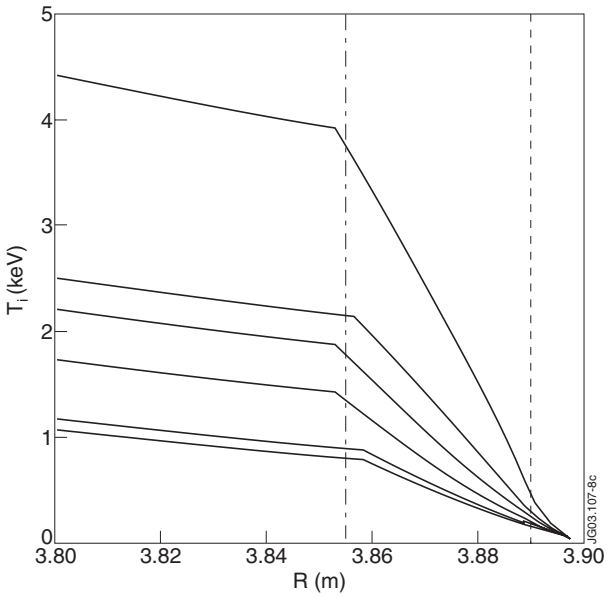

Figure 8: Ion temperature as a function of the major radius in integrated predictive simulations with different levels of external neutral gas puffing. Counting from top to bottom in the figure, the ion density profiles correspond are from simulations with the following levels of gas puffing: $\Gamma = 0$, $\Gamma = 2 \times 10^{22}$ s^{-1}, $\Gamma = 4 \times 10^{22}$ s^{-1}, $\Gamma = 6 \times 10^{22}$ s^{-1}, $\Gamma = 8 \times 10^{22}$ s^{-1}, $\Gamma = 2 \times 10^{23}$ s^{-1} and $\Gamma = 0$. The position of the top of the ETB has been indicated with a chain line and the separatrix with a dashed line.

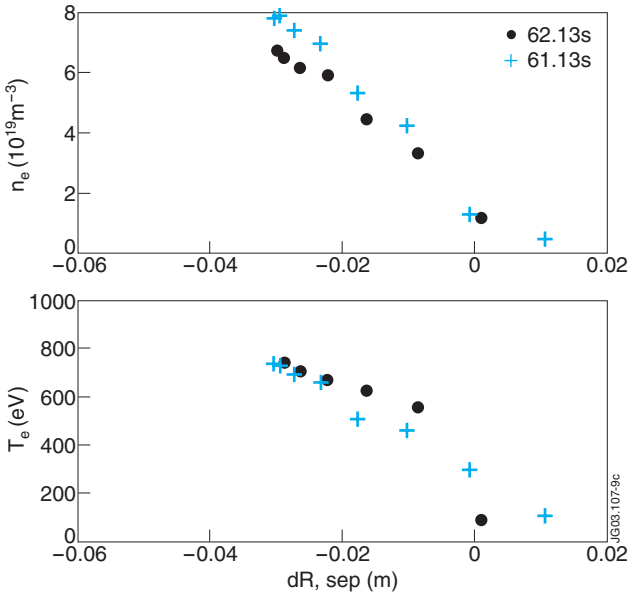

Figure 9: Edge Lidar data of the electron density and electron temperature in the vicinity of the separatrix for Pulse No: 53299 with an external gas fuelling rate of $\Gamma = 6 \times 10^{22}$ s^{-1}. The position of the separatrix is uncertain by a few centimetres. Therefore, the scale does not indicate the true distance to the separatrix.

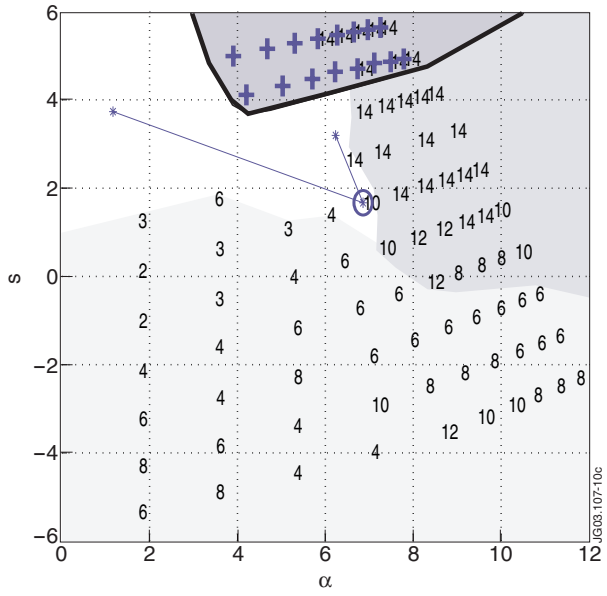

Figure 10: MHD stability diagram for the case with gas fuelling $\Gamma = 0$. The numbers indicate the mode number of the most unstable mode. The $n = \infty$ ballooning unstable region has been marked with crosses. The operational point has been plotted for $\rho = 0.92$ 0.95 and 0.99. The location of the top of the ETB at $\rho = 0{:}95$ has been marked with a circle.

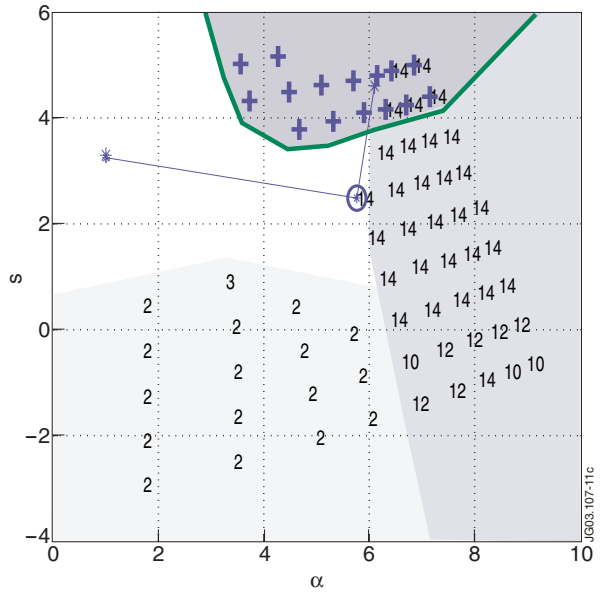

Figure 11: MHD stability diagram for the case with gas fuelling $\Gamma = 4 \times 10^{22}$ s^{-1} The symbols in the figure are to be interpreted as in Fig. 10. The operational point has been plotted for $\rho = 0.92$, 0.95 and 0.98.

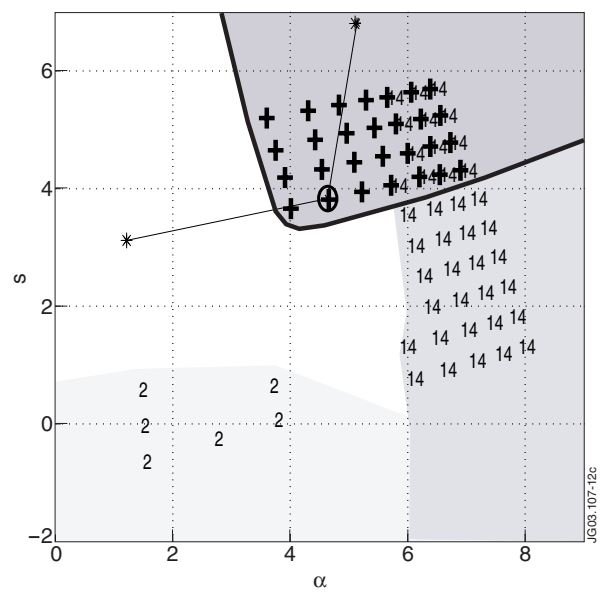

Figure 12: MHD stability diagram for the case with gas fuelling $\Gamma = 1 \times 10^{23}$ s^{-1}. The symbols in the figure are to be interpreted as in Fig. 10. The operational point has been plotted for $\rho = 0.92$, 0.95 and 0.98.

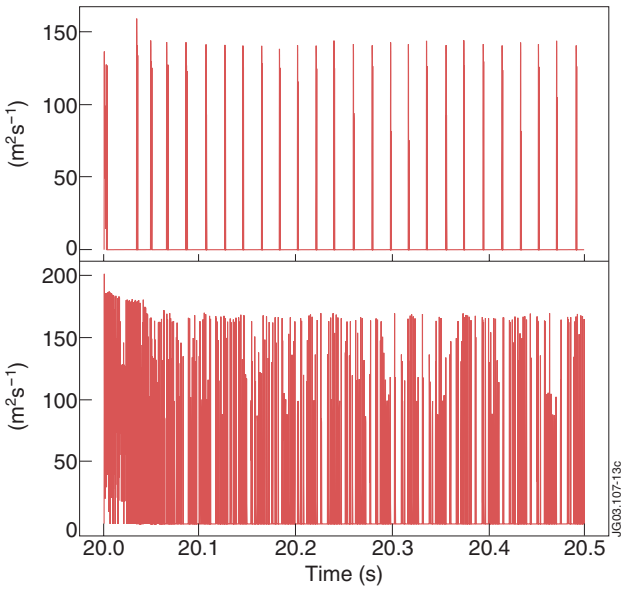

Figure 13: The ion thermal conductivity as a function of time in two JETTO simulations. (a) Gas puffing $\Gamma = 2 \times 10^{22}\ s^{-1}$ and critical pressure gradient $\alpha_c = 6$. (b) Gas puffing $\Gamma = 1 \times 10^{23}\ s^{-1}$ and critical pressure gradient $\alpha_c = 3{:}5$. The ELM frequencies are about 50 Hz and 500 Hz, respectively.

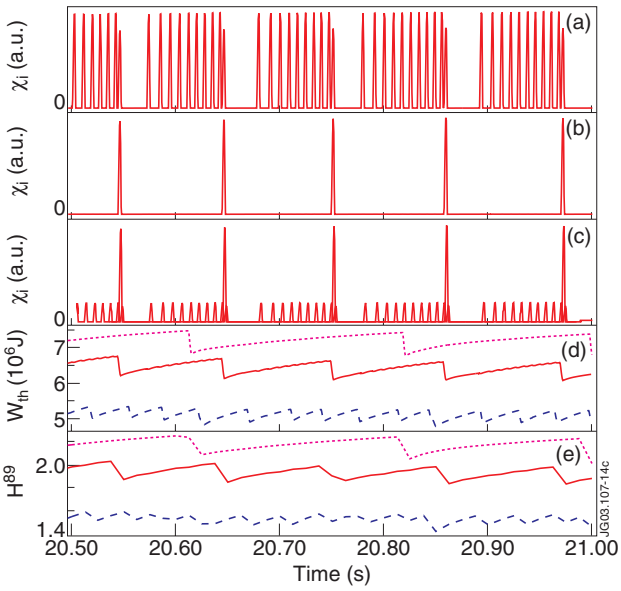

Figure 14: Mixed type I-II ELMy H-mode obtained in a JETTO simulation with a moderate level of gas puffing ($\Gamma = 4 \times 10^{22}\ s^{-1}$). The ETB was split into two parts: an innerregion with $\alpha_c = 6.0$ and an outer region with c = 3:5. (a) Ion thermal conductivity as a function of time showing the "small" type II ELMs in the outer region of the ETB. (b) Ion thermal conductivity as a function of time in the inner region of the ETB showing the "large" type I ELMs. (c) Composite ion thermal conductivity as a function of time. (d) Plasma energy content as a function of time. For comparison, the dotted curve corre-sponds to a simulation with pure type I ELMy H-mode ($\alpha_c = 6.0$) and the dashed curve to a simulation with pure type III ELMy H-mode ($\alpha_c = 3.5$). (e) Confinement factor H89 as a function of time. Again, the results for a case with type I ELMy H-mode (dotted curve) and type III ELMy H-mode (dashed curve) have been included.